# Electrical and Optical Characterization of Monolayer $WSe_2$ Field Effect Transistor

By

Qiang Yao
Master of Science

Physics

Ajit Srivastava
Advisor

Hayk Harutyunyan
Committee Member

Daniel Weissman
Committee Member

Zhigang Jiang
Committee Member

Accepted:

Lisa A. Tedesco, Ph.D.
Dean of the James T. Laney School of Graduate Studies

Date

# Electrical and Optical Characterization of Monolayer WSe2 Field Effect Transistor

By

Qiang Yao
B.S., Dalian University of Technology, 2016

Advisor: Ajit Srivastava, Ph.D

An abstract of
A thesis submitted to the Faculty of the
James T. Laney School of Graduate Studies of Emory University
in partial fulfillment of the requirements for the degree of
Master of Science
in Physics
2018

# Abstract

## Electrical and Optical Characterization of Monolayer WSe2 Field Effect Transistor

By Qiang Yao

Atomically thin transitional metal dichalcogenides (TMDs) encourage has attracted great attention due to its interesting optical and electrical properties. Similar to graphene, monolayer TMDs also have a honeycomb lattice structure with a two-atom basis. The band gap experiences a crossover from indirect to direct by reducing the thickness of the bulk TMDs to monolayers, which is promising for modern optoelectrical applications.

Excitons are electron-hole pairs bounded by Coulomb force with large a binding energy. When the excitons are trapped in the defects, localized quantum emitters [4] are formed, called quantum dots (QDs). To study the optical property of the QDs in monolayer TMDs, the photoluminescence spectra is utilized to observe the emission peaks and its gate voltage dependence. QDs in two dimensional TMDs have the potential to become highly efficient single photon emitters for future optoelectronics. In this thesis, I will show the electrical and optical measurement for the monolayer $WSe_2$, especially the emission property of several QDs.

The inversion symmetry breaking generates a valley contrasting Berry curvature in K and –K valleys. Berry curvature is the effective magnetic field in momentum space and generates the valley Hall effect. The subtraction of the magnetization current from the total current in the transport system gives rise to the thermal Hall effect. The thermal Hall effect causes a valley imbalance effect which breaks the time reversal symmetry. Magneto-optic Kerr effect (MOKE) is employed to detect this time reversal symmetry and a low temperature MOKE setup is proposed for the detection.

# Electrical and Optical Characterization of Monolayer WSe2 Field Effect Transistor

By

Qiang Yao
B.S., Dalian University of Technology, 2016

Advisor: Ajit Srivastava, Ph.D

A thesis submitted to the Faculty of the
James T. Laney School of Graduate Studies of Emory University
in partial fulfillment of the requirements for the degree of
Master of Science
in Physics
2018

# Contents

# Introduction

## Transitional metal dichalcogenides (TMDs)

Since the exciting advancement in the fabrication of graphene [1-3], two-dimension semiconductors have attracted great attention in modern condensed matter physics. The optical and transport properties of two-dimensional semiconductor materials remain the central part of modern optoelectronics. Transition-metal dichalcogenides (TMDs) are two-dimensional semiconductor materials with layered structures [4].

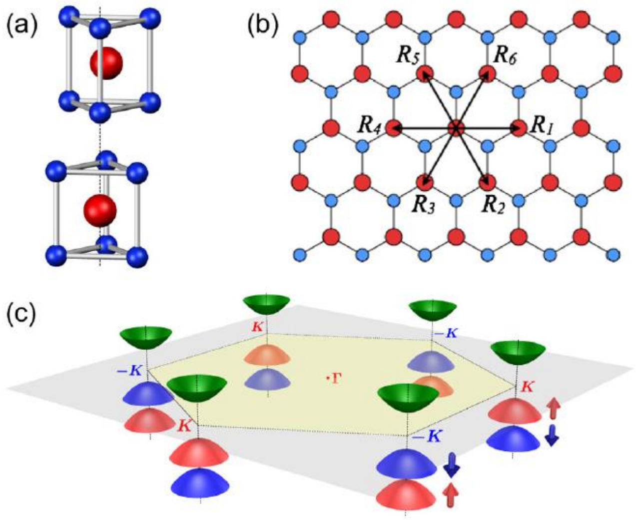

Fig.1 | (a) Stacking structure of bilayer TMDs, (b) honeycomb structure of monolayer TMDs, (c) direct band gap at six corners of momentum space, at K and -K valleys exhibit significant spin-orbital splitting exists in valence band with opposite spin orientations [9].

Similar to graphene, each TMD layer exhibits a honeycomb structure composed of a two-atom basis with the form of $MX_2$, in which M is the group VI (Mo, W) metal atom and X is the chalcogen atom (S, Se, Te). In the monolayer TMDs, the M atom layer is located in the middle of the two X atom layers which are the mirror reflection of each other. In the bulk form of TMDs or thin films with even number of layers, the inversion symmetry is preserved. While in the thin films with odd number of layers, the inversion symmetry is explicitly broken. The interlayer interaction between different layers is the van der Waals force, which is much weaker than the intralayer covalent bond. Such a layered structure makes it possible to mechanically exfoliate monolayers from TMD bulk materials [5-8].

The reciprocal lattice of the monolayer TMDs also has a honeycomb lattice structure with the six corners called K points [10-12]. These six corners are divided into two degenerate but inequivalent categories, K and K' points, because of the two-atom basis in monolayer TMDs. The K and K' points are time reversals of each other because of the symmetric lattice structure. Since the minimum of the conduction bands and the maximum of the valence bands are located at K and K' points for monolayer TMDs, they are usually called K and K' valleys [9,13].

The bandgap of a semiconductor is defined as the minimum energy difference between the lowest conduction band and the highest valence band. Due to the inherent inversion symmetric lattice structure, graphene has no band gap at K and K' points. In order to realize the tunability of the bandgap of graphene, a backgate voltage can be applied to a bilayer graphene or an epitaxial graphene to break the inversion symmetry [14,15]. The inversion symmetry is automatically broken in monolayer TMDs [9], which opens a finite band gap between the conduction band and the valence band. Remarkable, by lowering the layer numbers, the band gap of TMDs experiences a crossover from indirect to direct [16-18]. In monolayer TMDs, the direct bandgap is located at the K and K' points within the visible frequency scale, which provides a perfect platform for the bandgap engineering [19].

The first-principle calculations show that at K and K' valleys of monolayer TMDs, the conduction band edge is mainly from the $d_{z^2}$ orbitals of M atoms and the valence band edge is mainly from the $d_{x^2-y^2}, d_{xy}$ orbitals of M atoms [9,20] (X-p orbitals are also mixed, but with weak contributions). The wave functions for the conduction band and valence band are defined as follows [9]: $|\phi_c\rangle = |d_{z^2}\rangle$,

$$|\phi_v^\tau\rangle = \frac{1}{\sqrt{2}}\left(|d_{x^2-y^2}\rangle + i\tau_z|d_{xy}\rangle\right), \qquad (1)$$

where *c* (*v*) means conduction (valence) band, and $\tau_z$ is the valley index (+1 for K valley, -1 for K' valley). With the help of a massive Dirac fermion model, the Hamiltonian at K and K' valleys edges in monolayer TMDs is [9]

$$\hat{H} = at\left(\tau_z k_x \hat{\sigma}_x + k_y \hat{\sigma}_y\right) + \frac{\Delta}{2}\hat{\sigma}_z, \tag{2}$$

where $\hat{\sigma}$ is the Pauli matrix, *a* is the lattice constant, *t* is the effective hopping integral, $\Delta$ is the bandgap.

There exists a strong spin-orbit coupling (SOC) from the *d* orbitals of metal atoms giving rise to a spin splitting to the valence (conduction) band edges at K and K' valleys [9]. The spins are out of plane due to the mirror reflection symmetry existing in monolayer TMDs, i.e. the highest valence band has spin up and the second highest valence band has spin down (Fig. 2). The energy splitting is large at the valence band, 160meV for monolayer $MoS_2$ [21,22] and 400meV for monolayer $WSe_2$ [23,24]. The spin splitting is much smaller for conduction bands due to the vanishing of the intra-atomic $\boldsymbol{L}\cdot\boldsymbol{S}$ coupling of M-$d_0$ orbitals [25,26], which is the major component of conduction band SOC. The still existing spin splitting comes from the coupling of the $\mathrm{X}-p_{\pm 1}$ orbitals and $\mathrm{M}-d_{\pm 1}$ orbitals [25]. The spin splitting at conduction bands is reversed for $MoX_2$ and $WX_2$ because of the competition between the above two contributions [25,27].

Incorporating the spin orbit coupling, the Hamiltonian at K and K valleys is corrected as [9]

$$\hat{H} = at\left(\tau_z k_x \hat{\sigma}_x + k_y \hat{\sigma}_y\right) + \frac{\Delta}{2}\hat{\sigma}_z - \lambda\tau\frac{\hat{\sigma}_z - 1}{2}\hat{s}_z, \tag{3}$$

where $2\lambda$ is the spin splitting, and $\hat{s}_z$ is the spin matrix.

The large momentum separation greatly enhances the valley relaxation time between the K and K' valleys, allowing valley to be a firm binary index. The time reversal symmetry and the inversion symmetry breaking in monolayer TMDs require the spin splitting to be finite and opposite for K and K' valleys, i.e. the valence (conduction) band edge has opposite spin directions for K and K' valleys [9]. Therefore, the spin directions of the split valence (conduction) bands are locked with their valley index because of the large energy splittng and the prohibition of the spin flip between the two valence bands, known as spin-valley locking effect.

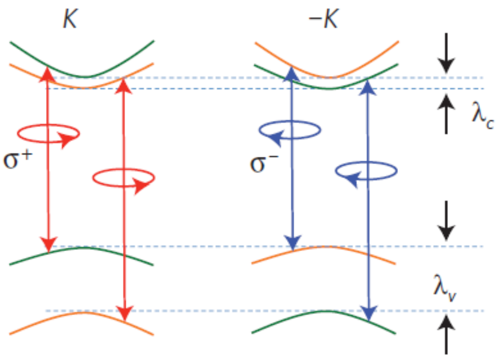

Figure.2| Spin splitting induced by the spin-orbital coupling and the resulting optical selection rules [29]

The inversion symmetry breaking in monolayer TMDs also generates the optical selection rules which indicates that a photon with $\sigma^+$ ($\sigma^-$) polarization only couples to the K (K') valley and emits a photon also with $\sigma^+$ ($\sigma^-$) polarization [9,13,28]. This selection rule can be used to detect and manipulate the valley coherence optically, making valley a promising information carrier [29].

## Excitons and quantum dots

The absorption of a photon can excite one valence band electron up to the above conduction band, leaving one hole behind in the valence band. The excited electron and the left hole compose a Hydrogen-like electron-hole pair bounded by the Coulomb force, known as exciton. Excitons play an active role in the study of optoelectronic properties of two-dimensional condensed matter systems. Excitons have a large binding energy due to reduced screening effect in the two-dimensional TMDs. The recombination of the electron-hole pair releases a photon determined by the band gap between the conduction and valence band. The exciton can be charged by a hole or an electron to become a charged exciton, known as trion. The energy of the neutral and charged excitons can be determined by various optical methods, such as photoluminescence (PL) spectra, reflection spectra [30-32], etc. The manipulation of the neutral and charged excitons can be achieved with the change of the sample control gate voltages [33]. The energy difference between the neutral excitons and the charged excitons reveals the binding energy of the excitons [30-32].

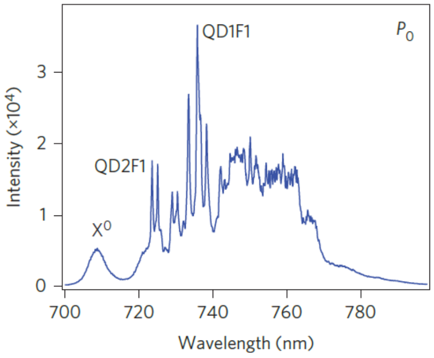

Fig. 3| Low-temperature PL spectra of a monolayer $WSe_2$ flake. $X^0$ is a free exciton peak and QD2F1, QD1F1 are two quantum dots [37].

When the excitons are trapped into the impurities of the materials, a zero-dimensional quasiparticle called quantum dot (QD) [34-36] is formed. Quantum dots play a significant part in multiple physical and chemical systems due to their remarkable optical and electrical properties. QDs are spatially localized and have lower energy than free excitons. The QDs can emit photons with specific frequencies due to their discrete electronic states and thus exhibit the characteristic of stable sharp peaks promising as single photon emitters with long lifetime of nanoseconds [37-40].

Fig. 3 shows the low-temperature PL spectra of a monolayer $WSe_2$ flake. On the red side of the broad exciton peak $X^0$, two sharp peaks labelled as QD2F1 and QD1F1 are located at the broad defects. Quantum dots' characteristic of zero-dimension, large binding energy, sharp peaks, and long lifetime make them highly efficient single photon emitters.

This report mainly discusses the quantum dots in monolayer $WSe_2$. The excitation energy is lower than the band gap of the monolayer $WSe_2$. The emission energy of the QDs is tunable by changing the gate voltage controlled doping density since the Fermi level is determined by the electron density of the sample. Gate voltage dependent PL spectra are observed to study the optical properties of multiple quantum dots.

### Berry phase effect and Valley Hall effect

Berry curvature is a local geometric quantity in k-space analogous to the magnetic field in real space, and its integral over a closed area in k space is the gauge-invariant Berry phase [41].

From a one-band theory, the general form of Berry curvature in Bloch bands is defined as [41]

$$\Omega_n(k) = \nabla_k \times \langle u_n(k)|i\nabla_k|u_n(k)\rangle, \qquad (4)$$

where $u_n(k)$ is the periodic part of the Bloch functions at n$^{th}$ band. In a two-dimensional semiconductor, the Berry curvature is perpendicular to the sample surface. The time reversal symmetry existing in K and K' valleys requires the Berry curvature to have identical magnitude but opposite signs $\boldsymbol{\Omega}(\boldsymbol{k}) = -\boldsymbol{\Omega}(-\boldsymbol{k})$, while the inversion symmetry forces the Berry curvature to have the same signs for K and K' valleys $\boldsymbol{\Omega}(\boldsymbol{k}) = \boldsymbol{\Omega}(-\boldsymbol{k})$ [13]. Therefore, the time reversal symmetry and inversion symmetry breaking are two necessary conditions for the Berry curvature to be valley contrasting [9].

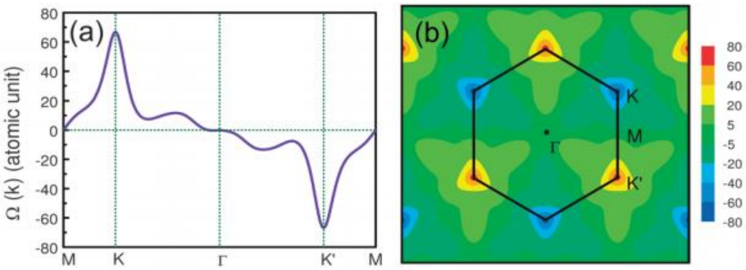

Fig. 4| First-principle calculation of the Berry curvature in monolayer $MoS_2$ [20]. The Bloch electrons at K (K') valleys feel an effective magnetic field pointing up.

The Berry curvature modifies the dynamics of electrons and thus the transport phenomenon. In the weak field limit, the semiclassical model for the equations of motion of the Bloch electrons is [42,43]

$$\dot{\boldsymbol{r}} = \frac{1}{\hbar}\frac{\partial E_n(\boldsymbol{k})}{\partial \boldsymbol{k}} - \dot{k} \times \boldsymbol{\Omega}_n(\boldsymbol{k}), \qquad (5)$$

$$\hbar\dot{\boldsymbol{k}} = -e\boldsymbol{E} - e\dot{\boldsymbol{r}} \times \boldsymbol{B}, \qquad (6)$$

where $E_n$ is the electron energy of *n*th band, $\boldsymbol{E}$ is the electric field, and $\boldsymbol{B}$ is the magnetic field.

It can be seen from equation (5) that the transport of the Bloch electrons includes two terms, the first term is the typical energy dispersion, the second term of $\dot{\boldsymbol{r}}$ is an anomalous velocity normal to an in-plane electric field (no magnetic field is applied) and the out-of-plane Berry curvature. Since the Berry curvature is valley contrasting, electrons from K and K' valleys are driven to opposite edges of the sample resulting in a transverse flow of valley pseudospin. This will cause an unbalanced valley distribution with K valleys accumulated at one side of the sample and K' valleys accumulated at the other side of the sample. This is so called valley Hall effect [13], which has been verified experimentally with an electrical method [44].

## Orbital magnetic moment and Thermal Hall effect

In momentum space, the Bloch electrons are wave packets, of which the self-rotation generate another valley contrasting quantity, the orbital magnetic momentum $\boldsymbol{m}$. Using a wave packet $|W_0\rangle = \int dqw(q,t)|\psi_n(q)\rangle$, where $|\psi_n(q)\rangle = e^{iq\cdot r}|u_n(q)\rangle$ is the Bloch function, the self-rotation of the wave packet gives [42,43]

$$\boldsymbol{m}(\boldsymbol{k}) = -(e/2)\langle W_0|(\boldsymbol{r}-\boldsymbol{r}_c)\times\boldsymbol{v}|W_0\rangle. \quad (7)$$

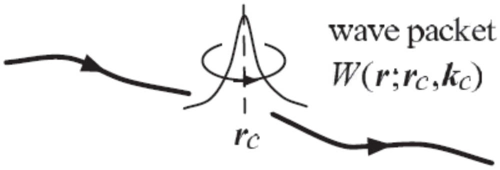

Fig. 5| A schematic drawing of the wave packet motion: the self-rotation of the wave packet around its center of mass, and the motion of its center of mass. [45]

After some algebra, the orbital magnetic moment $\boldsymbol{m}$ is expressed with the wave functions [42,43]

$$\boldsymbol{m}(\boldsymbol{k}) = -\mathrm{i}(e/2\hbar)\langle\nabla_{\boldsymbol{k}}u|\hat{H}(\boldsymbol{k})-\epsilon(\boldsymbol{k})|\nabla_{\boldsymbol{k}}u\rangle, \quad (8)$$

where $\widehat{H}(\boldsymbol{k})$ is the crystal Hamiltonian, $\epsilon(\boldsymbol{k})$ is the energy dispersion and the energy is corrected by $\boldsymbol{m}$: $\varepsilon_m = \varepsilon(\boldsymbol{k}) - \boldsymbol{m}(\boldsymbol{k}) \cdot \boldsymbol{B}$. In the massive Fermion model, the orbital magnetic moment is written as [13,29]

$$m(k) = -\hat{z}\frac{2a^2t^2\Delta}{4a^2t^2k^2+\Delta^2}\frac{e}{2\hbar}\tau_z. \tag{9}$$

Due to the time reversal symmetry and the inversion symmetry breaking, the magnetic moment $\boldsymbol{m}$ has nonzero but opposite magnitudes in different valleys leading to the Zeeman shift in a finite magnetic field [43]. In the following discussion about the thermal Hall effect, $\mathbf{m}$ plays a significant role to obtain the Hall current involving the temperature gradient.

In valley Hall effect, the electric field is a mechanical force driving the transport by changing the Hamiltonian of the Bloch electrons through correcting the electron velocity with the Berry curvature. On the other hand, statistical force, such as the temperature and chemical potential gradient, is also able to generate transport phenomenon macroscopically [34,37]. Inspired by the Onsager relation, people have been trying to find the Berry phase correction to the statistical force driven transport phenomenon, in which case the intrinsic anomalous velocity is missing due to the absence of the mechanical force.

A semiclassical wave packet method [45] is used to find the Berry phase effect to the temperature gradient driven transport. Given the orbital magnetic moment $\boldsymbol{m}$, the local current of a system in equilibrium is corrected with an extra term [46]

$$\mathbf{J} = -\mathrm{e}\int[d\boldsymbol{k}]g(r,k)\dot{r} + \nabla\times\int[dk]f(\boldsymbol{r},\boldsymbol{k})\boldsymbol{m}(\boldsymbol{k}), \tag{10}$$

where $g(\mathbf{r}, \mathbf{k})$ is the local statistical distribution, $[d\boldsymbol{k}] = d\boldsymbol{k}^2/(2\pi)^2$, the second term is the current from the self-rotation magnetization $\boldsymbol{M}^{self} = \int[d\boldsymbol{k}]f(\boldsymbol{r},\boldsymbol{k})\boldsymbol{m}(\boldsymbol{k})$, and $g(\mathbf{r}, \mathbf{k})$ is replaced by the Fermi-Dirac distribution $f(\mathbf{r}, \mathbf{k})$ for linear-order calculation [45].

In phase space, the Berry curvature $\boldsymbol{\Omega}$ modifies the density of states in a weak-field limit with the integral of a physical quantity $\mathcal{O}(\mathrm{k})$ written as [47]

$$\int [\boldsymbol{dk}](\mathbf{1} + \boldsymbol{e\Omega} \cdot \mathbf{B}/\hbar)\, \mathcal{O}(\mathrm{k}). \tag{11}$$

With the orbital magnetic moment modifying the energy dispersion, the magnetization density is thus derived with basic statistical mechanics involving the Berry phase effect [45]

$$\mathbf{M}(\mathbf{r}) = \int [d\boldsymbol{k}] f(\boldsymbol{r}, \boldsymbol{k}) \boldsymbol{m}(\boldsymbol{k}) + \frac{1}{\beta} \int [d\boldsymbol{k}] \frac{e}{\hbar} \boldsymbol{\Omega}(\boldsymbol{k}) log(1 + e^{-\beta(\varepsilon-\mu)}), \tag{12}$$

where $\beta = 1/k_B T$, $\mu$ is the chemical potential. The first term originates from the self-rotation of the electron wave packet, and the second terms originates from the motion of the center of the wave packet [48].

In a time-reversal symmetry breaking system, a temperature gradient generates both the observable transport charge (heat) current and the nonobservable circulating (heat) current [49] $\boldsymbol{\nabla} \times \mathbf{M}(\mathbf{r})$. However, the total current is the linear response of the external field [50] including the above two contributions. The subtraction of this nonobservable magnetization current from the local current $\mathbf{J}$ gives the transport current [45]:

$$\mathbf{j} = \mathbf{J} - \boldsymbol{\nabla} \times \mathbf{M}(\mathbf{r}), \tag{13}$$

Plugging in the magnetization $\mathbf{M}$ from equation (12), the transport current is given by [45]

$$\mathbf{j} = -\mathrm{e} \int [d\boldsymbol{k}] g(r, \boldsymbol{k}) \dot{\boldsymbol{r}} - \boldsymbol{\nabla} \times \frac{1}{\beta} \int [d\boldsymbol{k}] \frac{e}{\hbar} \boldsymbol{\Omega}(\boldsymbol{k}) \times log(1 + e^{-\beta(\varepsilon-\mu)}), \tag{14}$$

where the first term is the typical charge current from the mechanical force (electric field), and second term is the Berry-phase correction to the transport current. With only a temperature gradient applied, the charge current vanishes and the Berry-phase related term proportional to the temperature gradient as excepted [45]

$$\boldsymbol{j}_{in} = -\frac{\boldsymbol{\nabla} T}{T} \times \frac{e}{\hbar} \int [d\boldsymbol{k}] \boldsymbol{\Omega} \left[ (\varepsilon - \mu) f + k_B T log(1 + e^{-\beta(\varepsilon-\mu)}) \right], \tag{15}$$

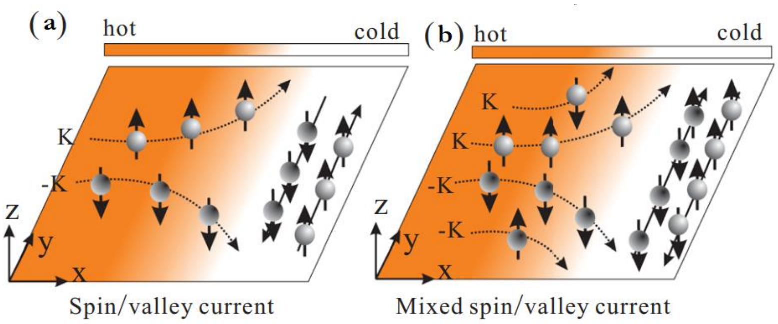

Fig. 6 | (a) A pure spin current and valley current is induced transverse to the in-plane temperature gradient, this happens when the Fermi level is located between the two spin-split conduction (valence) bands. (b) A mixed spin current is induced when the Fermi level is higher the higher conduction band or lower than the lower valence band, a pure valley current is still available. [51]

This expression indicates a Hall current transverse to the in-plane temperature gradient $\boldsymbol{\nabla} T$ and the out-of-plane Berry curvature $\boldsymbol{\Omega}$. Since the Berry curvature is opposite for K and K' valleys, the electrons from different valleys flow to opposite sides of the sample giving rise to a valley accumulation imbalance at the two edges. Consequently, the valley potential is tilted oppositely which explicitly breaks the time reversal symmetry locally at the edges. For a highly electron (hole) doped system, the charge and spin imbalance vanishes, leaving valley the only distinction between the two edges.

From equation (16), it is not hard to derive the temperature dependent anomalous Nernst conductivity (ANC) defined by $j_x = \alpha_{xy}(-\nabla_y T)$, [45]

$$\alpha_{xy} = -\frac{1}{e}\int d\varepsilon \frac{\partial f}{\partial \mu}\sigma_{xy}(\varepsilon)\frac{\varepsilon-\mu}{T}, \tag{16}$$

where $\sigma_{xy}(\varepsilon)$ is the zero-temperature anomalous Hall conductivity

$$\sigma_{xy}(\varepsilon) = -\frac{e^2}{\hbar}\int [dk]\Theta(\varepsilon - \varepsilon_k)\Omega_z(k). \tag{17}$$

At low temperatures, the ANC simplifies to the Mott relation

$$\alpha_{xy} = \frac{\pi^2}{3}\frac{k_B^2 T}{e}\sigma'_{xy}(\varepsilon_F). \tag{18}$$

The incorporation of the nonvanishing Berry curvature offers a Lorentz-like force to transport particles driven by mechanical forces or statistical forces, allowing valley pseudospin to be a promising index for electronics and caloritronics.

**Magneto-Optic Kerr Effect (MOKE)**

Due to the absence of net charge polarization in the Hall current from the thermal Hall effect, conventional electrical methods fail to probe the valley imbalance effect at the two edges of the sample. As mentioned above, the time reversal symmetry is locally broken at two edges of the sample. In this case, we will employ the magneto-optic Kerr effect (MOKE) to detect the existence of valence imbalance effect at the edges.

Magneto-optic Kerr effect (MOKE) [52] was first discovered by John Kerr in 1875 [53] and plays an important role in detecting the magnetization of materials. In analogy to the Faraday effect, the Kerr effect is defined as the polarization rotation when a normal linearly polarized light is reflected from a magnetized material, and the light obtains an ellipticity. The microscopic origin of MOKE is the spin-orbit coupling [54] induced Zeeman effect in a magnetized material, which causes the energy splitting of the transition states (two-level system) with different magnetic moments [55]. A linearly polarized light is the coherent superposition of a right circularly polarized light $\boldsymbol{\sigma}^+$ and a left circularly polarized light $\boldsymbol{\sigma}^-$ with the same magnitude. The incident $\boldsymbol{\sigma}^+$ and $\boldsymbol{\sigma}^-$ light experience different refraction indices $n_{L/R}$ and acquire a phase difference $\Delta\theta = (\omega L/c)(n_L - n_R)$ after reflecting from the medium. The polarization axis of the output light is thus rotated by an angle $\theta = \Delta\theta/2 = (\omega L/2c)(n_L - n_R)$ [56], where $\omega$ is the frequency of the incident light, $L$ is the sample thickness, $c$ is the speed of light in vacuum. Besides, the loss difference between $\sigma^+$ and $\sigma^-$ light renders their magnitudes different and gives rise to an ellipticity to the reflected light.

There are three types [57] of Kerr rotation effects based on the orientations of the magnetization of the materials, (1) polar Kerr effect, (2) longitudinal Kerr effect, (3) transverse Kerr effect. In this experiment, we only consider the polar Kerr effect with the magnetization perpendicular to the plane of the sample and thus the plane of the incident light. Polar Kerr effect has been successfully used to detect the valley Hall effect existing in the bilayer $MoS_2$ transistors [58] and the spin Hall effect [59,60] in GaAs. In the valley Hall effect experiment [58], the Kerr signal changes its sign with changing the doping types and increases linearly with relatively high bias voltages.

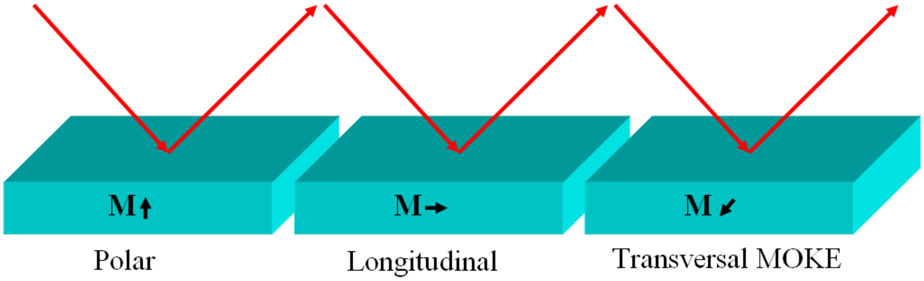

Fig. 7 | Three types of Kerr effects based on the orientation of the magnetization **M**. [57]

There exist other reciprocal effects which may change the polarization of the incident light. The distinction between the Kerr effect and other reciprocal effects is that the Kerr effect is originated from the time reversal symmetry breaking (TRSB) and the other effect are not [61]. The incident light reflected from a surface without TRSB will go back to its initial polarization state, while the light reflected from the surface with TRSB will experience a rotation angle. Therefore, MOKE is a significant method to detect the existence of the time reversal symmetry breaking in the materials. In this thesis, a low temperature MOKE setup will be proposed as a necessary training for future use.

## Experiments and results

### Monolayer $WSe_2$ field effect transistor

The monolayer $WSe_2$ flake mechanically exfoliated from the bulk $WSe_2$ onto a thick PMDS film and then transferred from the PDMS film to the $SiO_2/Si^{++}$ substrate with a dry method. The overall device is a field effect transistor (FET) structure designed as follows. The substrate is a p-doped Si layer covered by a $SiO_2$ layer, where the doped Si layer serves as the back gate. The dielectric layer of the device is the $SiO_2$ layer with a BN layer and the channel of the FET device is the monolayer $WSe_2$

flake. Spin coating is performed to cover the flake with positive photoresist. Then, scan electron microscopy and electron beam lithography are used to pattern the gold electrodes as the source and drain of the channel.

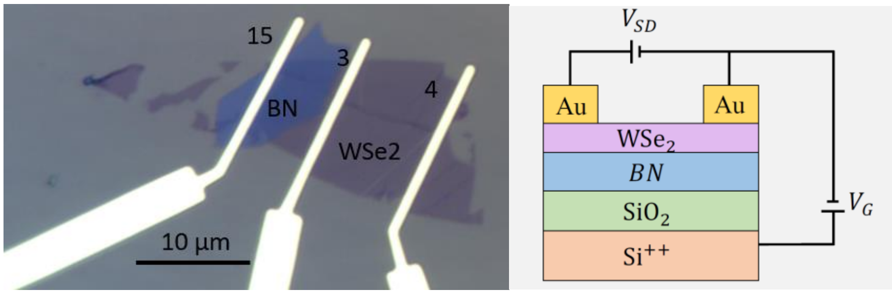

Fig. 8 (a) Optical microscope image of monolayer $WSe_2$ on top of BN layer, 3, 4, 15 are three Au contacts on the sample, (b) Schematic of field effect transistor (FET).

A back-gate voltage can be applied to the $Si^{++}$ substrate to change the doping level of the sample, and a bias voltage can be applied to the source and drain to induce current to the channel. In order to apply backgate voltage and bias current to the sample, wire bonding is performed to connect the electrodes on the flake and the substrate to the pins of the chip carrier. The FET device is mounted on a home-built low-temperature microscope in the He-4 cryostat at a low temperature (3.4 K). The xyz pizo stage (ANC300) is used to move the sample in the x, y, z directions in order to focus the laser spot and scan the incident position of the laser. A white light source () is used to view the position of the laser spot. The space-resolved PL spectra is integrated to locate the distributions of the QDs in the sample and determine the energies of the corresponding QDs (see Fig. 9 (a)).

The heater and the sensors of the attocube are used to change and measure the temperature near the sample respectively. To realize the control of the attocube and the cryostat with the control panel, careful wiring is required to connect the positioners, heater, and sensors of the attocube inside the cryostat. Thin copper wires are used for good conductivity. The pins in the chip carrier are then connected to the Keithleys, from which the current and voltage of the sample can be detected and controlled.

The $WSe_2$ monolayer flake is first identified using the optical microscope. The thickness of the $WSe_2$ flake can be measured by the atomic force microscopy (AFM) and confirmed by the photoluminescence (PL) spectra (Fig. 9(b)).

**Transport characterization**

The transport measurement is necessary to estimate the doping level of the sample. When $V_{bg}$ is positive (negative), the monolayer $WSe_2$ is electron (hole) doped, the major carriers are electrons (holes). The doped charges can be driven by the bias electric field ($V_{sd}$) to give the $I_{sd}$. Figure. 10 presents the source-drain current ($I_{sd}$) as a function of the back-gate voltage ($V_{bg}$) with both positive and negative source-drain voltage ($V_{sd}$). The gating curve exhibits an ambipolar transport phenomenon at both positive and negative $V_{sd}$, which means both p-doped and n-doped current can exist in our sample. When the $V_{bg}$ is low, no in-plane current can be seen. When the $V_{bg}$ goes lower than -70 V at p-doped region, the current starts to appear and increase sharply as expected. When $V_{bg}$ comes to zero, there is a hysteresis between forward and backward trace at both p-doped and n-doped regions.

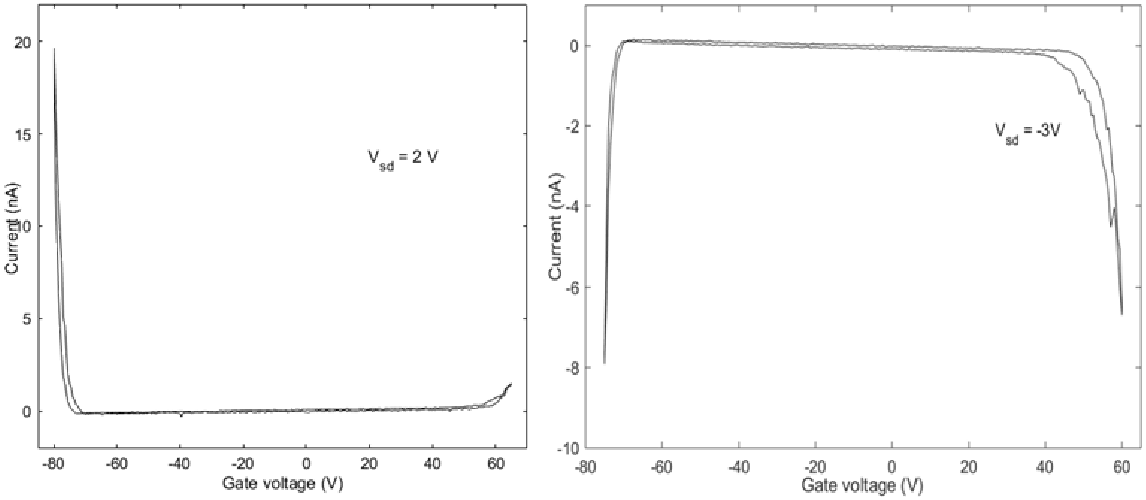

Fig. 10| Source-drain current ($I_{sd}$) as a function of back gate voltage ($V_{bg}$) at different source-drain voltages, (a) $V_{sd}$ = 3 V, (b) $V_{sd}$ = -2 V.

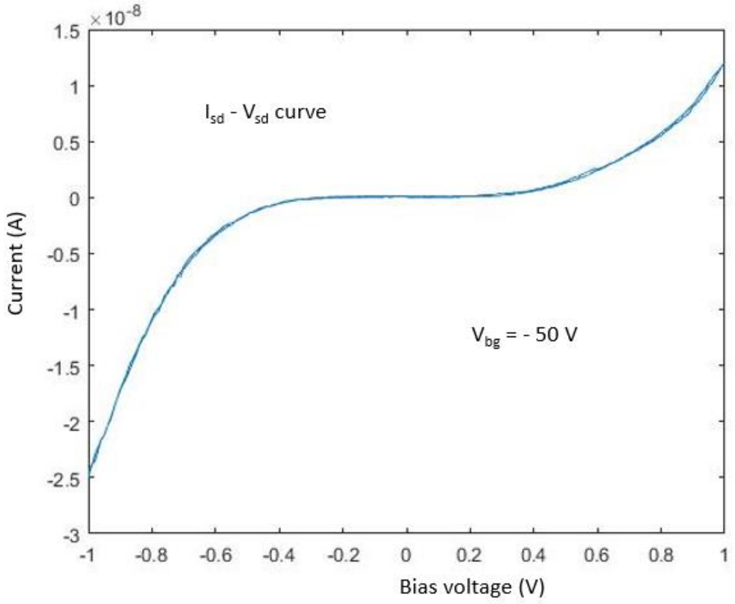

Fig. 11| Source-drain current as a function of the voltage applied on the monolayer $WSe_2$ by the source and drain. The back-gate voltage is set to be -50 V.

The source-drain current as a function of the bias voltage is measured with the $V_{bg}$ = -50 V, from which an obvious Schottky behavior is observed.

### Optical characterization

In a semiconductor system, an electron in the valence band can be excited to the conduction band by the photons with energy larger than the band gap energy, leaving a hole in the valence band. Since it is unstable for particles to stay at high-energy levels, the electron and hole in the conduction and valence band relax to the minimum energy state and recombine to release a photon. By detecting the energy of the photon, the photoluminescence (PL) spectra is obtained. Our laser sources are a Ti:S continuous wave laser and a HeNe (633nm) laser.

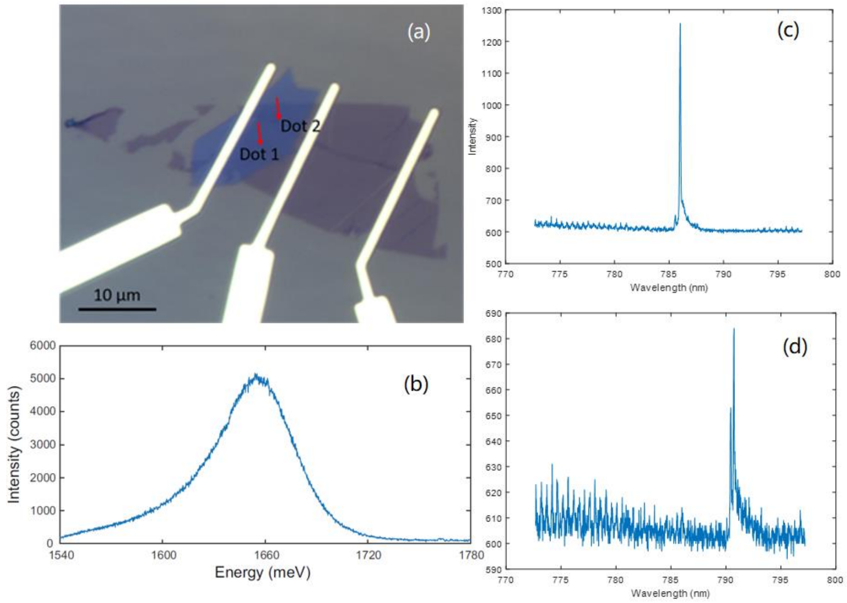

Fig. 9| (a) Spatial distribution of QDs in the monolayer WSe2 flake, QD1 and QD2, (b) room temperature PL of the exciton in monolayer $WSe_2$ flake, (c, d) PL spectra of two QDs, QD1 (786nm) and QD2 (790nm) at $V_{bg}$ = -80V.

The spatial distribution of the QDs in the sample is shown in Figure. 9 (a). Two significant quantum dots are found in the monolayer $WSe_2$ with different energies, QD1 (786nm), QD2 (790nm).

An obvious broad shoulder appears near the red side of the QD peak as a phonon side band effect. Along with the emission of the QDs, the excitation can excite a phonon lowering the emission energy of the QDs. The doublet on the blue side of the QD2 indicates that it is a neutral exciton.

## Power dependent PL spectra

The power dependent PL spectra are measured to demonstrate the origin of the emission peaks. For free excitons, the peak intensity is linearly proportional to the power of the excitation laser, in other words, the slope of the log-scaled power dependent PL spectra should be one. While for localized QDs, the emission intensity will saturate with the increase of the laser power so that the corresponding slope should less than one. The 786nm QD and the 790nm QD power dependent PL spectra are shown in Fig. 11, of which the slope of 0.81 and 0.61 respectively shows that they are localized quantum emitters.

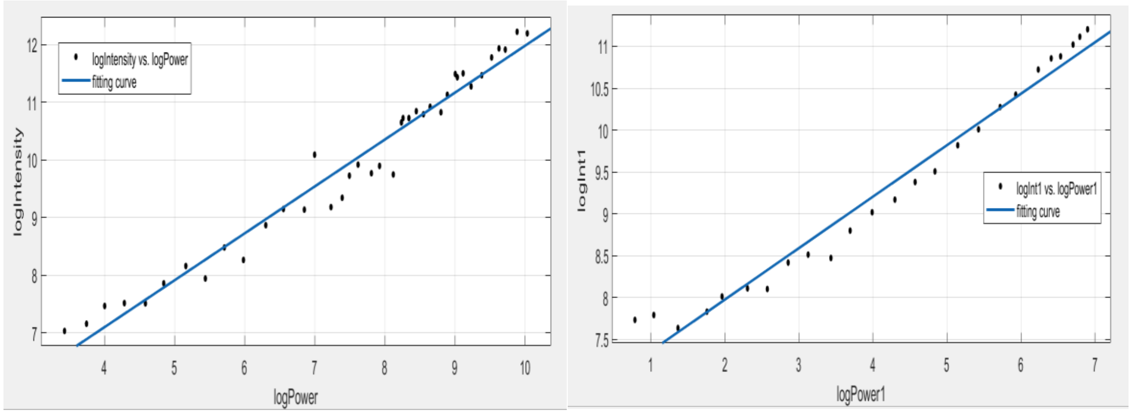

Fig. 12| PL peak intensity for QD1 and QD2 as a function of the excitation power with Vbg = -80V, 725nm laser. The slopes of the two fitting lines are 0.81 and 0.61.

### Backgate voltage ($V_{bg}$) dependent PL spectra

The $V_{bg}$ dependent PL spectra is performed to study the influence of the doping type and level on the three QDs. With higher back gate voltages, the sample is more electron doped and consequently the Fermi level is enhanced. In the experiment, the $V_{bg}$ first increases from 0V to 85V, and then decreases monotonously to -85V and finally comes back to 0V. All the three QDs only show up when the $V_{bg}$ is higher than certain values as a result of the depletion of the electrons of the sample.

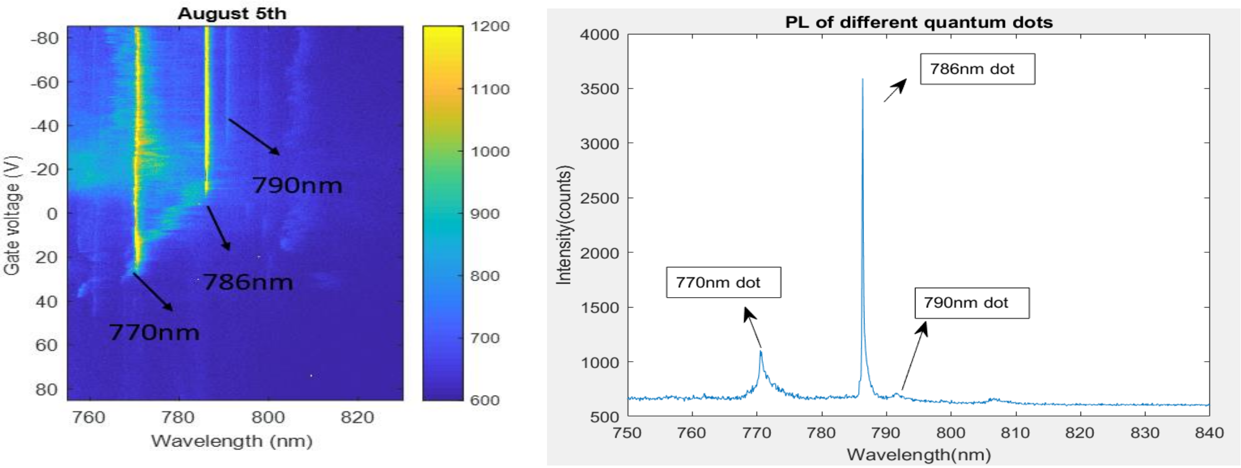

Fig. 13| Gate dependent PL spectra with three strong emission peaks (770 nm, 786 nm, 790 nm) from quantum dots.

We also performed the source-drain voltage ($V_{sd}$) dependent PL spectra to the 786nm dot, in which the $V_{sd}$ is the bias voltage applied along the sample. The following spectrum shows an asymmetric dependence between peak intensity and the $V_{sd}$. The PL completely disappears when $V_{sd}$ is -6 V, quite different from 6 V. We ascribe the disappearing of PL at -6 V to the decreasing of oscillator strength since the bias voltage could pull the wave functions of the electron and hole apart from their symmetric position. As for the asymmetry existing at 6 V and -6 V, the asymmetry of Schottky barrier for the source and drain might be one of the causes.

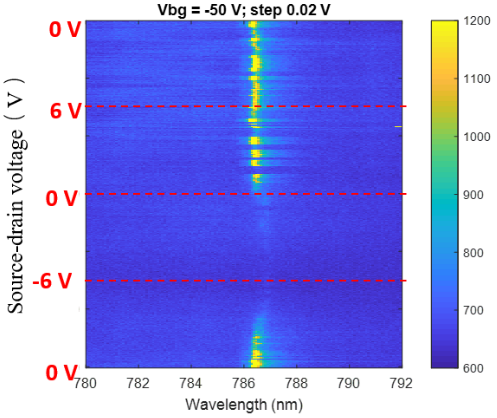

Fig. 14 | source-drain voltage dependence of PL spectra

### Photoluminescence excitation (PLE) spectroscopy

By tuning the wavelength of the excitation laser, the photoluminescence excitation (PLE) is measured to study the resonant property of QD1 and QD2. The measurements of the $V_{bg}$, $V_{sd}$ dependent PL spectra and the PLE spectroscopy are performed remotely with the help of the matlab programs. The programs can control the scanning of $V_{bg}$, $V_{sd}$, the excitation wavelength and, at the same time, measure the PL spectra.

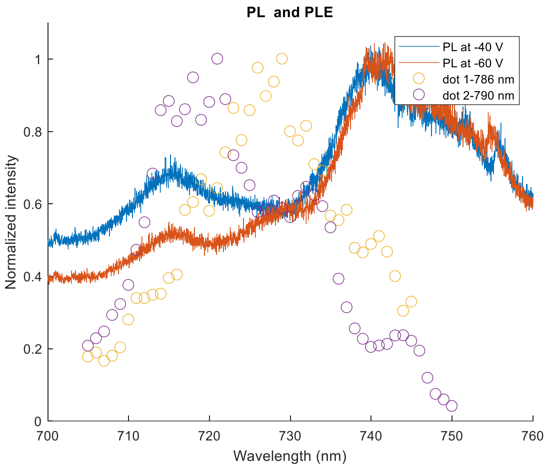

Fig. 15| PLE spectra of 786nm dot (orange circle) and 790nm dot (blue circle), PL spectra at -40 V (blue line) and -60 V (red line).

The excitation power is kept invariant (300 mW) throughout the whole measurement. The PLE spectra of QD1 and QD2 are plotted together with the PL spectra with two different back-gate voltages at low temperature. Two PL spectra are measured with different $V_{bg}$, which indicates different doping levels (See Fig. 14). When the Vbg is -40V, the peak at around 713nm corresponds to the free exciton in monolayer $WSe_2$. When the Vbg is -60V, a peak near the blue side of the broad defect peak (730nm) appears as a trion peak. The maximum intensity of the PLE of QD1 and QD2 correspond to the peak of free exciton and trion peak respectively, which implies that these two QDs are from the monolayer $WSe_2$ instead of the BN layer.

## Low temperature Kerr rotation setup

To detect the Kerr rotation at a low temperature, an optical setup is proposed. The detailed experiment principles are given followed by a brief introduction of relevant instruments.

When the time reversal symmetry is not broken, the Kerr rotation is missing. In this case, the half-wave plate before the Wollaston prism is adjusted to the orientation that the output light is 45° with respect to the main axis of the Wollaston prism, in which case the outgoing light is spitted into two linear lights with the same amplitude. Since the balanced photodiodes output the difference of these two lights, we expect a zero signal from the balanced photodetector. When the time reversal symmetry is broken by the valley imbalance effect at the opposite sides of the sample (either from the valley Hall effect or from the thermal Hall effect), a Kerr rotation is produced which rotates the reflected light by a Kerr angle $\delta\theta$. Consequently, the reflected light is no longer 45° to the Wollaston prism' optic axis and the two outcoming lights are different in magnitude $P_f = P_0\cos^2(\frac{\pi}{4} \pm \delta\theta), P_s = P_0\sin^2(\frac{\pi}{4} \pm \delta\theta)$.

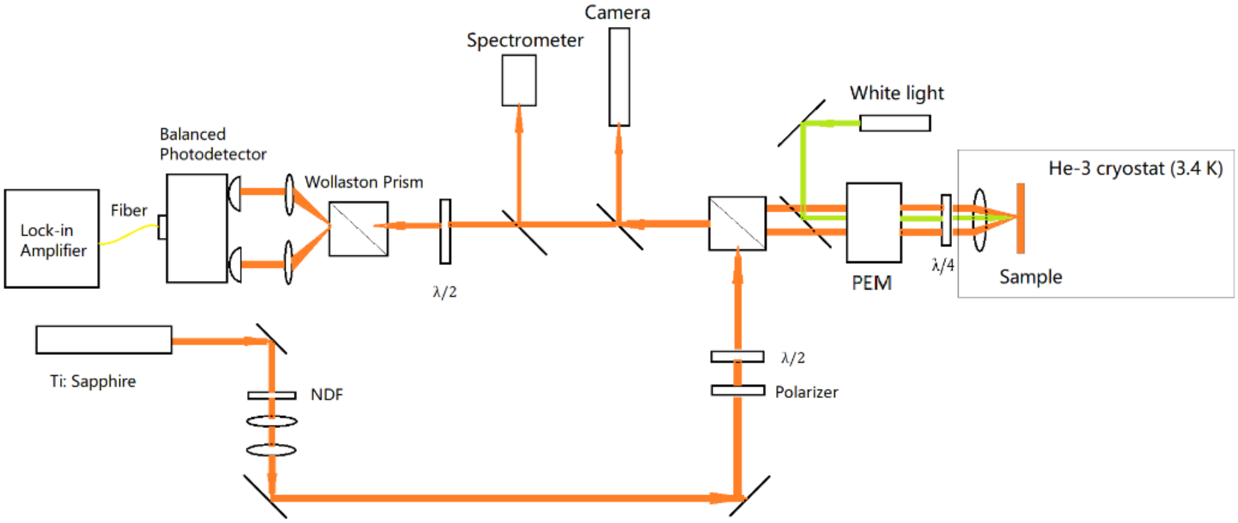

Fig. 16 | The experimental setup for the detection of the Kerr rotation induced by the thermal Hall effect.

*Photoelastic modulator*

The photoelastic modulator (PEM) can be used to modulate the laser polarization with a high frequency *f*. The output light from the PEM is changing between right circularly polarized $\sigma^+$ and left circularly polarized light $\sigma^-$. In our setup, a quarter-wave plate is mounted after the PEM to convert the $\sigma^+$ and $\sigma^-$ light back to two perpendicular linearly polarized lights respectively with the same frequency *f*. The typical frequency *f* is 50 kHz, and this frequency is set to be the reference frequency of the lock-in amplifier.

### *Wollaston prism*

Wollaston prism, composed of two triangle calcite prisms with perpendicular optic axes, can split a random light into two linearly orthogonal lights. Specifically, when the polarization of the incident light is normal to the optic axes of the two prisms, the two output lights have the same magnitude.

### *Balanced detector*

The two orthogonal lights coming from the Wollaston prism are collected by a balanced photodetector (PDB435A) and converted to an electrical signal (voltage). The output voltage is proportional to the power difference between the two input lights focus on the photodiodes.

### *Lock-in amplifier*

Lock-in is used to increase the sensitivity of the Kerr effect. Limited by the magnitude of the temperature gradient that we can apply, the Kerr expects to be small considering the noise signals. With the existence of other depolarization processes that could rotate the reflected light by an angle, a lock-in amplifier is used to extract the Kerr signal reducing the influence of the noises. The reference frequency of the Lock-in amplifier is set to (50 kHz). The change of the back-gate voltage modifies the doping density of the sample, which consequently changes the Kerr rotation angle. The back-gate voltage dependent Kerr angle can be used to estimate the noise.

## Conclusions

Transitional metal dichalcogenides (TMDs) are promising two-dimensional semiconductors, of which the crystal structure and the electronic band structure are introduced. The large direct band gap and the valley degree of freedom make the TMD monolayer a perfect platform for the study of optoelectronics in solid state physics. The inversion symmetry breaking lifts the degeneracy of K and K' valleys, giving rise to the consequent valley contrasting physics such as spin-valley locking and optical selection rules, making it possible to optically and electrically manipulate the valley coherence.

The exciton is a Hydrogen-like electron-hole pair bounded by the Coulomb force. When excitons are trapped into defects or impurities, they become zero-dimensional single photon emitters, known as quantum dots (QDs). QDs exhibit the characteristic of sharp peak, low energy and long lifetime.

The monolayer WSe2 flake is mechanically exfoliated from a bulk WSe2 and transferred on the SiO2/Si$^{++}$ substrate. The I-V relation of the FET device is studied, which shows an ambipolar transport phenomenon. In this article, two main QDs (786nm, 790nm) are found on the monolayer WSe2. Optically, PL spectra are measured at various back gate voltages to demonstrate the optical properties of these QDs. The peaks for the QDs only appear when the back-gate voltage is higher than a certain value. The PL spectra with varying the bias voltage is also presented showing an asymmetry for opposite voltages.

The inversion symmetry breaking also gives rise to the valley Hall effect, in which the Berry curvature is involved as effective magnetic field. Magneto-optic Kerr effect is directly from the time reversal symmetry breaking in the magnetized materials and has been employed to detect the valley Hall effect. Thermal Hall effect is the analogy to the valley Hall effect with the external electric field replaced by the temperature gradient. A low temperature MOKE setup is finally proposed to optically study the thermal Hall effect in monolayer TMDs.

## References

[1] K. S. Novoselov, A. K. Geim, S.V. Morozov, D. Jiang, Y. Zhang, S.V. Dubonos, I.V. Grigorieva, and A. A. Firsov, Science **306**, 666 (2004).

[2] K. S. Novoselov, A. K. Geim, S.V. Morozov, D. Jiang, M. I. Katsnelson, I.V. Grigorieva, S.V. Dubonos, and A. A. Firsov, Nature (London) **438**, 197 (2005).

[3] Y. Zhang, Y.-W. Tan, H. L. Stormer, and P. Kim, Nature (London) **438**, 201 (2005).

[4] Q. Wang et al., Nature Nano. **7**, 699 (2012)

[5] K. S. Novoselov, D. Jiang, F. Schedin, T. J. Booth, V. V. Khotkevich, S. V. Morozov and A. K. Geim, Proc. Natl. Acad. Sci. **102**, 10451 (2005).

[6] A. Splendiani, L. Sun, Y. Zhang, T. Li, J. Kim, C.-Y. Chim, G. Galli and F. Wang, Nano Lett. **10**, 1271 (2010).

[7] K. F. Mak, C. Lee, J. Hone, J. Shan and T. F. Heinz, Phys. Rev. Lett. **105**, 136805 (2010).

[8] B. Radisavljevic, A. Radenovic, J. Brivio, V. Giacometti and A. Kis, Nat. Nanotechnol. **6**, 147 (2011).

[9] D. Xiao, G.-B. Liu, W. Feng, X. Xu, W. Yao, Phys. Rev. Lett. **108**, 196802 (2012).

[10] T. Li and G. Galli, J. Phys. Chem. C **111**, 16192 (2007).

[11] S. Lebegue and O. Eriksson, Phys. Rev. B **79**, 115409 (2009).

[12] Z.Y. Zhu, Y. C. Cheng, and U. Schwingenschlo¨gl, Phys. Rev. B **84**, 153402 (2011).

[13] D. Xiao, W. Yao, Q. Niu, Phys. Rev. Lett **99**, 236809 (2007).

[14] T. Ohta *et al.*, Science **313**, 951 (2006).

[15] E. McCann and V. I. Fal'ko, Phys. Rev. Lett. **96**, 086805 (2006); E.V. Castro *et al.*, arXiv:cond-mat/0611342; H. Min, B. Sahu, S. K. Banerjee, and A. H. MacDonald, Phys. Rev. B **75**, 155115 (2007).

[16] Li, T. & Galli, G. J. Phys. Chem. C **111**, 16192 (2007).

[17] Lebègue, S. & Eriksson, O. Phys. Rev. B **79**, 115409 (2009).

[18] Zhu, Z. Y., Cheng, Y. C. & Schwingenschlögl, U. Phys. Rev. B **84**, 153402 (2011).

[19] Conley, H. J. et al. Nano Lett. **13**, 3626 (2013).

[20] G.-B. Liu, D. Xiao, Y. Yao, X. Xu, W. Yao, Chem. Soc. Rev., **44**, 2643 (2015).

[21] Mak, K. F., Lee, C., Hone, J., Shan, J. & Heinz, T. F., Phys. Rev. Lett. **105**, 136805 (2010).

[22] Ross, J. S. et al., Nature Commun. **4**, 1474 (2013).

[23] Zhao,W. et al., ACS Nano **7**, 791_797 (2013).

[24] Zeng, H. et al., Sci. Rep. **3**, 1608 (2013).

[25] G.-B. Liu, W. Y. Shan, Y. Yao, W. Yao, D. Xiao, Phys. Rev. B **88**, 085433 (2014).

[26] A. Kormanyos, V. Zolyomi, N. D. Drummond et al., Phys. Rev. B **88**, 045416 (2013).

[27] K. Kosmider, J. W. Gonzalez, J. Fernandez-Rossier, Phys.Rev. B **88**, 245436 (2013).

[28] Xiao, D., Liu, G-B., Feng,W., Xu, X. & Yao,W., Phys. Rev. Lett. **108**, 196802 (2012).

[29] X. Xu, W. Yao, D. Xiao, T. F. Heinz, Nature Physics **10**, 343 (2014).

[30] Jones, AM, Yu, H and Ghimire, NJ et al., Nat Nanotechol **8**, 634 (2013).

[31] Ross, JS,Wu, S and Yu, H et al., Nat Commun **4**, 1474 (2012).

[32] Mak, KF, He, K and Lee, C et al., Nat Mater **12**, 207 (2012).

[33] H. Yu, X. Cui, X. Xu, W. Yao, National Science Review **2**, 57 (2015).

[34] DiVincenzo, D. P., Fortschr. Phys. **48**, 771 (2000).

[35] Imamoglu, A. et al., Phys. Rev. Lett. **83**, 4204 (1999).

[36] Gao, W-B., Fallahi, P., Togan, E., Miguel-Sanchez, J. & Imamoglu, A., Nature **491**, 426 (2012).

[37] A. Srivastava et al., Nature Nanotech. **10**, 491 (2015).

[38] Y. –M. He et al., Nature Nanotech. **10**, 497 (2015).

[39] M. Koperski et al., Nature Nanotech. **10**, 503 (2015).

[40] C. Chakraborty et al., Nature Nanotech. **10**, 507 (2015).

[41] D. Xiao, M.-C. Chang, Q. Niu, Rev. Mod. Phys. **82**, 1959 (2010).

[42] M.-C. Chang, Q. Niu, Phys. Rev. B **53**, 7010 (1996).

[43] G. Sundaram, Q. Niu, Phys. Rev. B **59**, 14915 (1999).

[44] K. F. Mak, K. L. McGill, J. Park, P. L. McEuen, Science **344**, 1489 (2014).

[45] D. Xiao, Y. Yao, Z. Fang, Q. Niu, Phys. Rev. Lett. **97**, 026603 (2006).

[46] D. Culcer, J. Sinova, N. A. Sinitsyn, T. Jungwirth, A. H. MacDonald, Q. Niu, Phys. Rev. Lett. **93**, 046602 (2004).

[47] D. Xiao, J. Shi, Q. Niu, Phys. Rev. Lett. **95**, 137204 (2005).

[48] L. F. Zhang, New J. Phys. **18**, 103039 (2016).

[49] T. Qin, Q. Niu, J. Shi, Phys. Rev. Lett. **107**, 236601 (2011).

[50] R. Kubo, J. Phys. Soc. Japan **12**, 570 (1957); R. Kubo, M. Yokota, S. Nakajima, ibid., p. 1203.

[51] X.-Q. Yu, Z.-G. Zhu, G. Su, A.-P. Jauho, Phys. Rev. Lett. **115**, 246601 (2015).

[52] S. Sugano, N. Kojima, eds., Magneto-optics. Berlin: Springer, 2000.

[53] J. Kerr, on rotation of the plane of polarization by reflection from the pole of a magnet, Philos. Mag. **3** (1877).

[54] E. du Tremolet de Lacheisserie, Magnetisme T. 1, EDP Sciences, 401 (2000).

[55] T. Haider, ijea, **7**(1), 17 (2017).

[56] P. M. Oppeneer, Handbook of Magnetic Materials, **13**, edited by Buschov K.H.J., Elsevier Science, (2001).

[57] Magneto-optic Kerr effect, Wikipedia, http://en.wikipedia.org/wiki/Magneto-optic_Kerr_effect

[58] J. Lee, K. F. Mak, J. Shan, Nature Nanotechnol. **11**, 421 (2016).

[59] Y. K. Kato, R. C. Myers, A. C. Gossard, D. D. Awschalom, Science **306**, 1910 (2004).

[60] V. Sih et al., Nature Phys. **1**, 31 (2005).

[61] A. D. Fried, Phys. Rev. B **90**, 121112 (R) (2014).